JOURNAL OF OPTOELECTRONICS AND ADVANCED MATERIALS Vol. 9, No. 1, January 2007, p. 99 - 105

Invited Lecture

High-resolution electron microscopy studies of metal nanoparticles: shape and twin defects, and surface stress effects

H. HOFMEISTER
Max Planck Institute of Microstructure Physics, Weinberg 2, D-06120 Halle, Germany

Potential applications of metal nanoparticles, because of specific physical or chemical properties, are in close relationship to their structural peculiarities. Structural characterisation of nanoparticles in various configurations, using high resolution electron microscopy (HREM), may reveal detailed information on particle shape and planar lattice defects. The variations observed for most noble metals comprise single crystalline particles of cuboctahedral shape, particles containing single twin faults, multiply twinned particles containing parallel twin lamellae, and particles composed of cyclic twinned segments arranged around axes of fivefold symmetry. Nanoparticles with free surface exhibit, because of their large surface-to-volume ratio, a size-dependent lattice contraction due to the surface stress. For spherical particles, the lattice contraction is a function of their radius. Thus, it can be calculated from the lattice spacings determined by HREM. In the case of strong interaction with a surrounding matrix, underlying support, or oxide coating, additional misfit stresses occur which contribute to an effective interface stress causing a larger lattice contraction, or even lattice dilatation. In the latter case the interface stress may take on negative values, which limits the curvature of the interface and for very small particles favours a self-limitation of their oxidation.

(Received November 28, 2006; accepted December 21, 2006)

Keywords: Metal nanoparticles, Electron microscopy, Particle shape, Twin defects, Surface stress

1. Introduction

The structural characteristics of metal nanoparticles become more and more important, because of structure-sensitive properties like mechanical strength [1], magnetism [2], chemical reactivity [3], or optical absorption [4]. For particles of transition metals like Pd, Ag, Au having sizes well below 10 nm, most routes of synthesis produce a great variety of particle shapes accompanied by variations of the internal structure [5]. This multitude of configurations may be understood in terms of the great ease of structural transformations during particle growth [6]. Besides single crystalline particles that may exhibit the shapes of truncated octahedra or cuboctahedra, single twinned particles of both shapes are found. The formation of twin faults, where the twin plane forms a boundary between the twinned subunits situated in mirror symmetry to each other, is a characteristic of face centered cubic (fcc) metal nanoparticles [7]. Such contact twins may form via nucleation or as a result of erroneously attaching atoms or molecules to a close packed plane during growth. Repeated twinning on parallel planes results in a linear arrangement of parallel lamellae with two alternating orientations, while on nonparallel coplanar planes it produces a circular arrangement of cyclic twins around fivefold axes [8-10].

The formation of metal nanoparticles in a matrix may be accompanied by the generation of tensile or compressive stresses due to thermal expansion mismatch [11]. The lattice spacings of crystalline nanoparticles sensitively reflect their state of stress, depending on the respective formation conditions [12-13]. Nanoparticles with free surface may exhibit, solely due to their small dimensions and because of their large surface-to-volume ratio A/V, a considerable lattice contraction Δa where the responsible hydrostatic pressure Δp is related to the surface stress f. For isotropic solids, f consists of the specific free surface energy γ and the contribution of elastic deformation to a reversible surface variation $f = \gamma + A\cdot d\gamma/dA$. For spherical fcc metal particles of radius r, the capillary pressure Δp is given by $\Delta p = 2f/r$, from which, with the compressibility $\kappa = -\Delta V/(V\cdot\Delta p)$, the lattice contraction $\Delta a = -2a\kappa f/3r$ is obtained as function of the radius of curvature r. Thus, f may be calculated from the size-dependent lattice contraction determined by means of HREM [14]. For anisotropic solids, f is the mean value of the various crystal facets forming the surface of the nanoparticle. For nanoparticles embedded in a matrix of foreign material, the surface stress f must be replaced by the interface stress f_i representing the elastic response of the interface between both materials to elastic deformation.

This paper is aimed at giving an overview on a variety of forms of metal nanoparticles by various routes of fabrication, as studied by HREM. The issue of the surface stress of metal nanoparticles is treated by HREM image diffractogram analysis of lattice plane fringes.

2. HREM investigation

HREM imaging enables structural characterization down to the atomic scale by interference of un-diffracted and diffracted electron beams. Typical image contrast peculiarities of nanoparticles concern surfaces, interfaces, stoichiometry variations, lattice distortions, thickness changes, and deviations from the bulk lattice symmetry [15]. The complex nature of image formation in the HREM mode limits a straightforward and intuitive interpretation of the resulting image contrast. However, the lateral extension of particles and the presence of some lattice defects can be deduced from lattice plane imaging with one or more sets of lattice plane fringes of a certain zone axis orientation.

Metal nanoparticles, either prepared for electron microscopy from solution on holey carbon-coated copper grids [14], or from a bulk matrix by appropriate thinning procedures [16] have been investigated using a JEM 4010 operating at 400 kV accelerating voltage. Images were recorded at optimum defocus settings (near Scherzer focus). Real space and reciprocal (Fourier) space image processing, using commercial Digital Micrograph and public domain NIH Image [17] software, were applied to digitized selections of micrographs for contrast enhancement and image evaluation. Since the Fourier transform (diffractogram) exhibits the spectrum of spatial frequencies present in an image, it can be used for analysing individual nanoparticles. There is a number of factors affecting the accuracy of lattice spacing determination by this technique [18], however a reasonable reliability of data is achieved when some selection criteria are carefully followed [19].

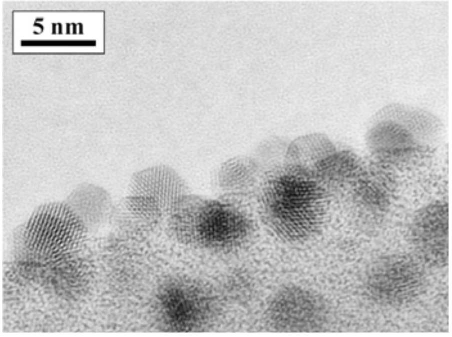

Fig. 1. HREM overview image of Au nanoparticles on the surface of a Stöber silica nanosphere.

3. Shape and twin defects

For nanoparticles of transition metals like Ni, Pd, Pt, and Cu, Ag, Au having a face centred cubic (fcc) lattice, most routes of synthesis produce a variety of particle shapes based on a cuboctahedron accompanied by variations of the internal structures due to planar defects [5,20]. In Fig. 1, a HREM overview of Au nanoparticles on Stöber silica [14] is shown, from which one can recognize that imaging of lattice plane fringes is best for those particles situated at the very rim of the projected silica nanosphere image. The particles exhibit a nearly cuboctahedral shape with distinct crystallographic facets rather than those of spheres. This is also observed for single crystalline Ag particles in glass, as can be seen from Fig. 2 where the profile correponding to a cuboctahedral shape of particles in (110) orientation is outlined by white lines [16]. Fig. 3 shows the diffractogram corresponding to Fig. 2, with an indication of the involved reflections emphasizing the single crystalline nature of that particle.

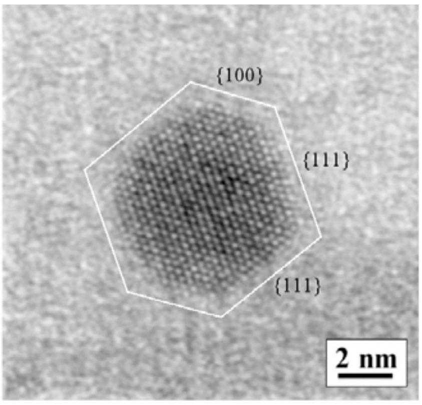

Fig. 2. Single crystalline Ag nanoparticle in glass imaged in (110) orientation with white lines marking the {111} and {100} planes.

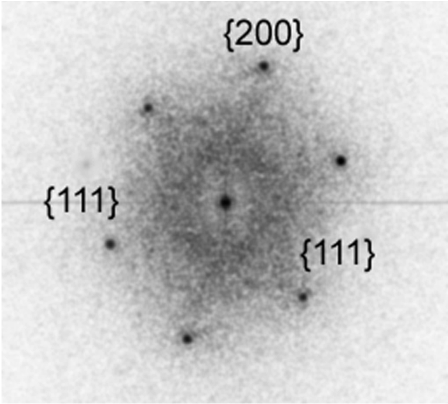

Fig. 3. Diffractogram corresponding to Fig. 2

The formation of twin faults, where the twin plane represents a boundary between the twinned sub-units situated in mirror symmetry to each other, is characteristic for these nanoparticles. They may form via nucleation or as result of erroneously attaching atoms to the particle lattice during growth. Repeated twinning on parallel planes produces parallel twin lamellae, whereas multiple twinning on alternate coplanar planes produces cyclic twin segments arranged around fivefold axes [8-10]. The atomic models of an un-twinned and a single twinned particle of truncated octahedron shape, shown in Fig. 4, may explain how one is derived from the other by reflecting its upper half at a horizontal atomic plane of {111} type in the center marked by arrows. This mirror plane is called the twin plane or twin boundary

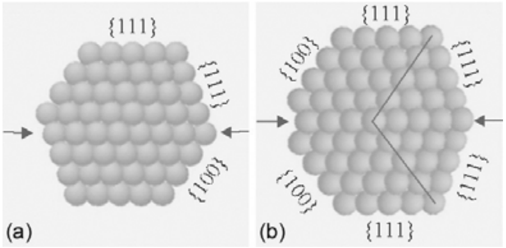

Fig. 4. Atomic models of (a) a cuboctahedron particle in (110) orientation without, and (b) with a twin fault, where arrows mark the plane along which the lattice of (a) is mirrored.

because it separates two regions of the particle having different lattice orientation. In <110> zone axis orientation used to represent the models of Fig. 4, the twin plane is seen end-on, and the two twin segments situated side-by-side exhibit the same orientation, but nearly 72° azimuthally rotated. This is indicated by the bend in the line drawn along a {100} plane.

An example for this configuration is given in Fig. 5 (a) that shows an Au nanoparticle where arrows indicate the twin boundary that belongs to one set of {111} planes common to both twin segments. As mentioned above, the metal nanoparticles considered also may contain more than one twin fault. Parallel twin lamellae by repeated twinning may have thicknesses as small as only three atomic layers [16,20]. The more twin planes are involved in the particle composition, the more complicated is the interpretation of the lattice fringe patterns, and the evaluation of lattice spacings because of superposition of several twin lamellae or segments. Unambiguous lattice analysis is only possible if the twin planes have cozonal orientation and are imaged end-on, as it applies to the twinned nanoparticles shown in Fig. 5.

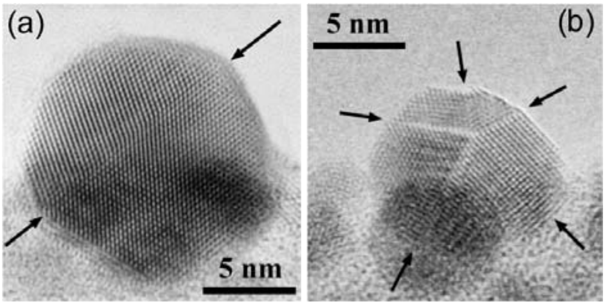

Fig. 5. HREM images of (a) a single twinned Au nanoparticle, and (b) a fivefold-twinned Ag nanoparticle on silica nanospheres with the twin boundaries indicated by arrows.

Another type of regular configuration with simple twin faults is found for multiple twinning on nonparallel coplanar twin planes. In fcc metals, low energy twin planes are of {111} type that enclose an angle of 70.53°, being close to 2π/5. Therefore, in these materials fivefold twinning may occur with cyclic twinned segments, leading to a pentagonal bi-pyramid shape [9]. Identification of such twin configurations requires a special high symmetry orientation with respect to the electron beam. An example of a nanoparticle with such a configuration is shown in Figure 5(b). Each of the five twin segments situated in <110> zone axis orientation always shares two coplanar {111} faces, the twin planes, with adjacent segments. The common inner edge of all segments of this decahedron, the fivefold twin junction, is oriented parallel to the electron beam, enabling a clear representation of the internal structure. Although in this case evaluation of the spacings and angular relations of the {111} and {200} type lattice plane fringes by means of diffractogram analysis revealed no deviation from the fcc lattice of the twin segments it is recommended not to consider such particles for lattice spacing evaluation [16]. This is even more correct with cyclic multiply twinned particles of icosahedron shape composed of 20 equi-sized twin segments of tetrahedron shape sharing 6 fivefold axes and one common corner at the center [9]. The features of HREM image contrast of such nanoparticles always result from double diffraction effects, due to superposition of two or more twin segments.

4. Surface stress effects

The state of stress of metal nanoparticles sensitively depends on their surface either being free or in contact to a surrounding coating or matrix, or to an underlying support of foreign material. Even the adsorption of specific molecules may affect their respective behaviour [21]. As mentioned above, the effects of surface stress and interface stress, respectively, are the more pronounced the smaller the particles are. For many materials, they become significant for sizes smaller than 10 nm [22]. The reason is the increasing ratio of the number *D* of surface atoms to the total number of atoms in a particle. This ratio, also called dispersion, reflects the increasing role of surface atoms with decreasing size, for a range of properties like optical absorption and chemical reactivity. For particles of a given geometry like the cuboctahedral model shown in Fig. 6 (a), being composed of completely filled shells of atoms, the number of atoms at the surface as well as the total number of atoms may be calculated according to polynomial expressions [23,24]. The evolution of the dispersion of cuboctahedral nanoparticles with size is represented by the bent curve in Fig. 6 (b), that may be compared to the linear evolution of the diameter of Ag nanoparticles of corresponding sizes given by the straight curve (right y-axis). From this representation it comes clear that an Ag nanoparticle of about 2 nm size containing about 310 atoms exhibits a dispersion of slightly above 0.5, i.e. more than half of the atoms are situated at the very surface.

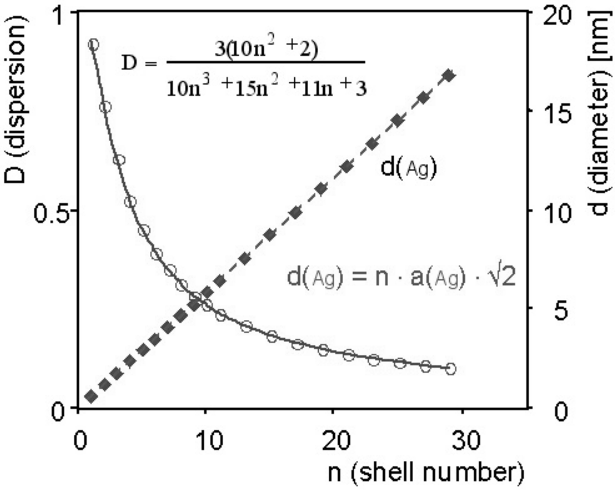

Fig. 6. Surface atoms to total atoms number ratio (a) in an 11 shells cuboctahedron particle model, and (b) as function of the number of filled shells drawn together with the corresponding particle diameter for Ag.

The capillary pressure Δp, inversely proportional to the particle radius r, causing isolated spherical particles to be in a state of compression, is balanced by the surface stress f if no additional forces are active: $\Delta p 4\pi r^2 = f 8\pi r$. As mentioned above, the induced elastic strain $\Delta a/a$ is related to Δp such that this linear relationship may be used to evaluate the surface stress from measurements of size-dependent lattice spacings. This was done for Ag and Au nanoparticles formed on Stöber silica nanospheres by a chemical impregnation procedure [25]. Lattice plane spacings were derived from the distance of {111} spots, as shown in Fig. 3 in the diffractograms of HREM images of single-crystalline nanoparticles. For these calculations, bulk modulus (i.e. the inverse compressibility) values of $B(Ag) = 1.036 \times 10^{11}$ N/m^2, and $B(Au) = 1.709 \times 10^{11}$ N/m^2 have been applied [26]. From the linear relation between the lattice spacing $D\{111\} = a/\sqrt{3}$ and the inverse particle radius $1/r$, as shown in Fig. 7, surface stress values of 2.55 ± 1.38 N/m for Ag nanoparticles and of 3.88 ± 1.45 N/m for Au nanoparticles have been obtained. The lattice spacings extrapolated to disappearing surface curvature deviate less than 1% from the respective bulk value. Surface stress values reported in the literature for both metals lie between 1.18 and 6.4 N/m [14]. From our results, we may conclude that the Ag and Au nanoparticles on silica nanospheres do not exhibit any strong metal-support interaction or adsorbate induced effects.

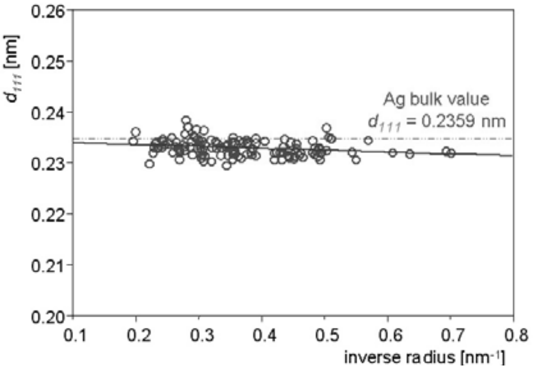

Fig. 7. Spacing of {111} lattice planes as a function of the inverse size of Ag nanoparticles (the horizontal line marks the bulk value).

Such effects seriously affecting the lattice spacings of metal nanoparticles rather are observed with crystalline oxide support, coating or matrix materials like alumina, ceria and magnesia [27]. Differences in the lattice structure and in the vibrational and bonding properties may cause lattice misfit, as well as thermal and elastic mismatch as possible sources of non-ideal accommodation of deposit nanoparticles on a substrate of foreign material. The induced effects are proportional to the contact area at the interface and to the strength of interaction across to it. In the case of nanoparticles coated by, or embedded in, a shell or matrix, respectively, of another phase, the contact area is increased to the whole nanoparticle surface becoming the interface. The stresses associated with these interfaces may predominantly concern the nanoparticles only, either due to their very small size or because of special properties of a coating shell.

The formation of misfit stress is frequently observed in the initial stage of epitaxial thin film growth on oxide substrates, characterized by a strong metal-support interaction where for metal nanoparticles smaller than a certain threshold of about 3 nm size, full accommodation of the metal lattice to the support lattice occurs [28]. For the general case of a misfitting sphere within a matrix, the above force equilibrium must be completed by a misfit stress σ^M, thus $\Delta p 4\pi r^2 = f 8\pi r + \sigma^M 4\pi r^2$ is attained where the right hand side of this equation may be considered as resulting from an effective interface stress f_i^{eff}. This is what can experimentally be derived from the elastic strain by measuring the lattice spacings: $f_i^{eff} = -(3r/2\kappa) \times (\Delta a/a)$.

Elastic strains with distinct contributions from interface-induced misfit stress, in addition to size effects, have been observed in various metal nanoparticles supported on oxide substrates like Ag on MgO(100) studied by X-ray absorption spectroscopy as well as Pt, Ta and Pd on $Al_2O_3(111)$, studied by transmission electron microscopy (TEM) [29-32]. In particular, nanoparticles of the latter metals exhibit upon epitaxial growth by physical vapour deposition drastic decreases of lattice parameters with decreasing particle size in the range 6 nm to 1 nm. The largest effect of about a 10% decrease has been observed by Klimenko et al. [30] for Pt nanoparticles of sizes ranging from 3 to 1 nm. To make these results comparable to those presented above the lattice parameter / particle size data pairs have been taken from

Fig. 6 of [30] and plotted in the same manner as the data of Ag on silica shown in Fig. 7. In this way Fig. 8 enables one to derive

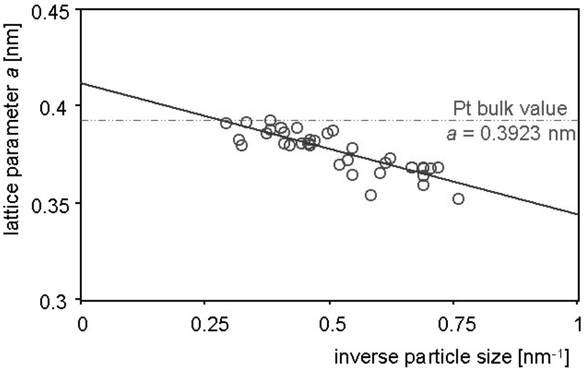

Fig. 8. Lattice parameter as a function of the inverse size of Pt nanoparticles taken from Fig. 6 of [30] (the horizontal line marks the bulk value).

from the slope of the linear data fit the effective interface stress obviously being active in the reported study as f_i^{eff} = 34.165 N/m where a bulk modulus value of *B(Pt)* = 2.760 × 10^{11} N/m^2 has been applied. This interface stress, considerably contrasting with the surface stress of ‘free’ Pt nanoparticles reported to lie in the range 2.574 to 5.165 N/m [22,33,34], must be understood in terms of a lattice misfit as large as 9.66%.

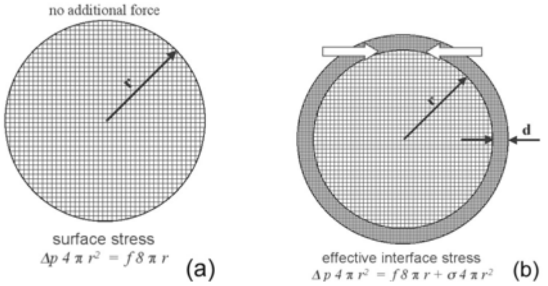

Fig. 9. Schematic representation of an isolated nanoparticle of spherical shape (a)where upon formation of an oxide coating (b) a misfit stress σ occurs (to accommodate the core - shell mismatch) that is contributing to an effective interface stress.

5. Oxide shell formation

A completely different behaviour may occur if an interface-induced misfit evolves together with the formation of a shell around the nanoparticles, due to a chemical surface reaction like oxidation that simultaneously reduces the particle size by metal consumption during the process. A description of the state of stress of such nanostructures, as shown in Fig. 9, must not only consider the effect of the stress due to the lattice misfit between metal and oxide, but also the spatial constraints caused by the oxide layer formation

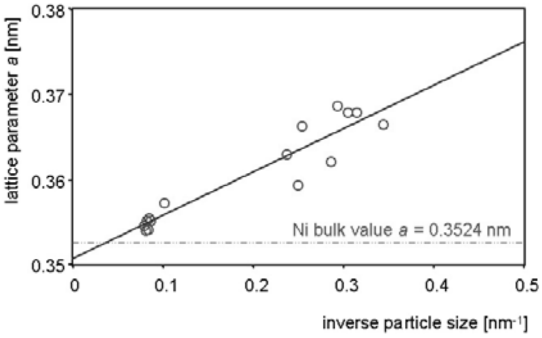

Fig. 10. Lattice parameter as a function of the inverse size of oxide-coated Ni nanoparticles taken from Fig. 7 of [34] (horizontal line: Ni bulk value).

in a spherical configuration. While the misfit stress σ^M depends on the radius *r* of the metal particle, a possible stress build-up in the oxide layer is proportional to the shell thickness *d*. If the lattice misfit requires a widening of the metal lattice to match with the larger oxide lattice spacings, a size dependent lattice dilatation should be found. This has been reported by Rellinghaus et al. [34] for the oxidation of Ni nanoparticles in ambient air. To compare their data to the others already presented here, the data pairs of lattice parameter and particle size have been taken from Fig. 7 of [35] and re-plotted as Fig. 10. From the slope of the linear data fit, an effective interface stress of f_i^{eff} = -17.5 N/m has been obtained, using a bulk modulus value of *B(Ni)* = 1.760 × 10^{11} N/m^2. For non-oxidized Ni nanoparticles, however, one would expect a positive surface stress of 2.24 N/m [36]. The sign and magnitude of the effective interface stress must be explained in terms of the rather large lattice misfit of 15.49%. By comparison of Fig. 8 and Fig. 10, as well as the corresponding data of lattice misfit and effective interface stress, it comes clear that in the evolution of stresses of oxide-coated Ni nanoparticles there are effective also contributions from the oxide shell.

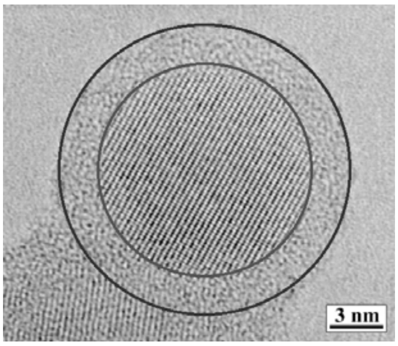

Fig. 11. HREM image of an oxide coated Si nanoparticle with the crystalline core and the amorphous shell marked by concentric circles.

From observations like those mentioned above, and from the finding that for a number of materials the oxide shell thickness decreases with decreasing particle size, an essential role of stress in the self-limiting oxidation of nanoparticles has been concluded [37-41]. The oxidation of Si nanoparticles fabricated by laser pyrolysis of silane under ambient conditions in air [38] is a good example to illustrate this behaviour. From the HREM image shown in Fig. 11, it can be recognized that the crystalline Si core is coated by a thick amorphous silicon oxide shell. For particles of a mean size of 7.45 ± 4.20 nm, the oxide thickness ranges from 0.8 to 2.9 nm, where a linear relationship between particle radius r and oxide shell thickness d could be observed. The spacings of the {111} lattice plane fringes, as a function of the inverse particle size, are shown in Fig. 12. From the slope of the linear data fit, an effective interface stress of $f_i^{eff} = -5.33$ N/m was derived using $B(Si) = 9.784 \times 10^{10}$ N/m^2 as the bulk modulus [26]. This result is within the range of surface stress data reported for the adsorption of oxygen on Si (111) [42]. Although the evaluated interface stress has a negative sign, which implies a limitation of the curvature that the interface can withstand for energetic reasons, and which may be understood as one of the reasons for a self-limitation of the oxidation of Si nanoparticles, it does not cause a lattice dilatation for particles of all sizes, as is the case for the oxide coated Ni nanoparticles shown above. Indeed, compressive stresses build up in the oxide shell that may partly counterba-lance the dilatation due to the core/shell mismatch. This is another reason for slowing down the oxidation process. Only for particle sizes below about 3 nm is the compressive effect of the oxide coating small enough, because of the reduced oxide shell thickness, to allow for a lattice dilatation.

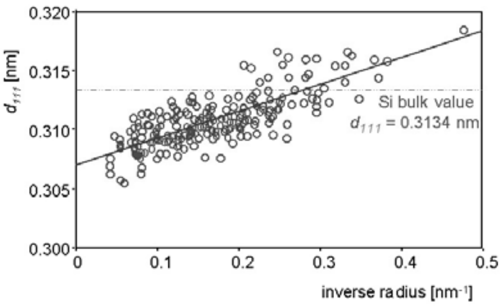

Fig. 12. Spacing of {111} lattice planes as a function of the inverse size of Si nanoparticles (the horizontal line marks the bulk value).

6. Conclusions

High-resolution electron microscopy structural characterisation of metal nanoparticles may provide detailed knowledge not only on their shape variations and planar defect content, but also on their state of stress and interaction with surrounding support, coating or matrix. This has been introduced and discussed by a number of examples like Ni, Pt, Ag, Au and Si. Imaging of lattice plane fringes and analysis of the corresponding diffractograms does not only provide crystallographic information on shape and internal structure of such nanoparticles in various configurations. It also allows one to detect size-dependent lattice parameter variations and, based on this, to classify the strength of interaction with the surrounding medium. Further on, the role of stress in the evolution of shell formation by surface reactions may be monitored. Thus, not only structure-property relations, but also the conditions of synthesis and processing may be optimised this way.

References

[1] Y.F. Shen, L. Lu, Q.H. Lu, Z.H. Jin, K. Lu, Scr. Mater. **52**, 989 (2005).
[2] F. Aguilera-Granja, J.M. Montejano-Carrizales, A. Vega, Solid State Commun. **133**, 573 (2005).
[3] C. Mohr, H. Hofmeister, P. Claus, J. Catal. **213**, 86 (2003).
[4] W.P. Cai, H. Hofmeister, M. Dubiel, Europhys. J. D **13** 245 (2001)
[5] L.D. Marks, Rep. Prog. Phys. **57**, 603 (1994).
[6] S. Iijima, J. Electron Microscopy **34**, 249 (1985).
[7] S. Iijima, and T. Ichihashi, Materials Transactions JIM **31**, 582 (1990).
[8] J.M. Montejano-Carrizales, J.L. Rodríguez-Lopéz, C. Guiterrez-Wing, M. Miki-Yoshida, M. José-Yacaman, in Encyclopedia of Nanoscience & Nanotechnology, ed. H.S. Nalwa, American Scientific Publ., Stevenson Ranch (2004), vol. 2, p. 237.
[9] H. Hofmeister, in Encyclopedia of Nanoscience & Nanotechnology, ed. H.S. Nalwa, American Scientific Publ., Stevenson Ranch (2004), vol. 3, p. 431.
[10] J. Urban, in Encyclopedia of Nanoscience & Nanotechnology, ed. H.S. Nalwa, American Scientific Publ., Stevenson Ranch (2004), vol. 10, p. 161.
[11] H. Hofmeister, M. Dubiel, H. Goj, S. Thiel, J. Microsc. **177**, 331 (1995).
[12] M. Dubiel, H. Hofmeister, E. Schurig, Rec. Res. Devel. In Appl. Phys. **1**, 69 (1998).
[13] M. Dubiel, H. Hofmeister, E. Schurig, E. Wendler, W. Wesch, Nuclear Instr. Meth. Phys. Res. B **166-167**, 871 (2000).
[14] H. Hofmeister, P.-T. Miclea, M. Steen, W. Mörke, H. Drevs, Topics in Catalysis, in press (2006).
[15] H. Hofmeister, in Nanostructured and Advanced Materials, eds. A. Vaseashta, D. Dimova-Malinovska, J.M. Marshall, Springer, Dordrecht (2005), p. 115.
[16] H. Hofmeister, M. Dubiel, G.L. Tan, K.-D. Schicke, Phys. Stat. Sol. (a) **202**, 2321 (2005).
[17] W. Rasband, 'NIH Image' public domain software. (http://rsb.info.nih.gov/nih-image/).
[18] P.A. Crozier, S.-C.Y. Tsen, J. Liu, C. Lopez Cartes, J.A. Perez-Omil, Jpn. J. Electron Microsc. **48** (1999) 1015.
[19] P.A. Crozier, S.-C.Y. Tsen, J. Liu, Ultramicroscopy **98** (2003) 63.

[20] H. Hofmeister, G.L. Tan, M. Dubiel, J. Mater. Res. **20**, 1551 (2005).
[21] A. Yanase, H. Komiyama, Surf. Sci. **226**, L65 (1990).
[22] R. C. Cammarata, K. Sieradzki, Ann. Rev. Mater. Sci. **24**, 215 (1994).
[23] R. van Hardeveld, F. Hartog, Surf. Sci. **15**, 189 (1969).
[24] J.M. Montejano-Carrizales, J.L. Móran-López, Nanostruct. Mater. **1**, 397 (1992).
[25] H. Hofmeister, P.-T. Miclea, W. Mörke, Part. Part. Syst. Charact. **19**, 359 (2002).
[26] Smithells Metals Reference Book, ed. E.A. Brandes, G.B. Brook, Elsevier Publ., Amsterdam (1998).
[27] F. Ernst, Mater. Sci. & Eng. **R14**, 97 (1995).
[28] C.R. Henry, Progr. Surf. Sci. **80**, 92 (2005).
[29] P. Lagarde, S. Colonna, A.-M. Flank, J. Jupille, Surf. Sci. **524**, 102 (2003).
[30] M. Klimenko, S. Nepijko, H. Kuhlenbeck, M. Bäumer, R. Schlögl, H.-J. Freund, Surf. Sci. **391**, 27 (1997).
[31] S. Nepijko, M. Klimenko, H. Kuhlenbeck, D. Zemlyanov, D. Herein, R. Schlögl, H.-J. Freund, Surf. Sci. **412/413**, 192 (1998).
[32] S. Nepijko, M. Klimenko, M. Adelt, H. Kuhlenbeck, R. Schlögl, H.-J. Freund, Langmuir **15**, 5309 (1999).
[33] H.J. Wasserman, J.S. Vermaak, Surf. Sci. **32**, 168 (1972).
[34] R.J. Needs, M.J. Goodfrey, M. Mansfield, Surf. Sci. **242**, 215 (1991).
[35] B. Rellinghaus, S. Stappert, E.F. Wassermann, H. Sauer, B. Spliethoff, Eur. Phys. J. D **16**, 249 (2001).
[36] J. Wan, Y.L. Fan, D.W. Gong, S.G. Chen, X.Q. Fan, Modelling Simul. Mater. Sci. Engn. **7**, 189 (1999).
[37] H. Hofmeister, P. Ködderitzsch, NanoStructured Mater. **12**, 203 (1999).
[38] H. Hofmeister, F. Huisken, B. Kohn, Eur. Phys. J. D **9**, 137 (1999).
[39] J. Dalla Torre, J.L. Bocquet, Y. Limoge, J.P. Crocombette, E. Adam, G. Martin, T. Baron, P. Rivallin, P. Mur, J. Appl. Phys. **92**, 1084 (2002).
[40] C.-H. Chen, T. Yamaguchi, K.-I. Sugawara, K. Koga, J. Phys. Chem B **109**, 20669 (2005).
[41] H. Coffin, C. Bonafos, S. Schamm, N. Cherkashin, G.B. Assayag, A. Claverie, M. Respaud, P. Dimitrakis, P. Normand, J. Appl. Phys. **99**, 044302 (2006).
[42] D. Sander, H. Ibach, Phys. Rev. B **43**, 4263 (1991).

---

[*] Corresponding author: hof@mpi-halle.mpg.de